



Characterization of wear properties of the functionally graded material deposited on cast iron by laser-aided additive manufacturing

Yongfeng Liu¹ · Fei Weng² · Guijun Bi² · Youxiang Chew² · Shibo Liu² · Guangyi Ma³ · Seung Ki Moon⁴

Received: 7 October 2018 / Accepted: 30 January 2019 / Published online: 12 February 2019
© Springer-Verlag London Ltd., part of Springer Nature 2019

Abstract

In this study, functionally graded material (FGM) was deposited on cast iron substrate by laser-aided additive manufacturing (LAAM). Inconel 625 nickel-base superalloy was firstly deposited on the substrate as a buffer layer, on which the stainless steel 420 (SS420) layers were subsequently prepared. The cracking issue was successfully eliminated in the deposited materials. With the optimized process parameters, the FGM with thickness up to 4.0 mm was achieved without cracks and other obvious defects. The SS420 layers showed fine dendritic microstructure derived from the rapid cooling rate of the LAAM process. Wear test results indicated that the FGM shows excellent wear resistance, especially under lubricated condition.

Keywords Functionally graded material · Inconel 625 · Stainless steel 420 · Cast iron · Wear resistance

1 Introduction

Cast irons are a large group of materials which can be divided into four types based on the graphite morphology: white cast iron, gray cast iron, malleable cast iron, and nodular cast iron. Among which, nodular cast iron has been widely applied in automotive engines, marine engines, heavy duty gears, and military and railroad vehicles, owing to the advantages of high ductility, good fatigue strength, wear resistance, shock resistance, and high modulus of elasticity [1–3]. Though casting can be used to fabricate very large and complex components,

such as those in marine engines, it is deemed environmentally unfriendly due to the generation of waste pollutions, emission of particles and dust, and harmful and poisonous gases. In this case, it is environmentally friendly and cost-effective to repair the damaged components compared with fabricating a new one by casting. Therefore, repair of damaged cast iron parts is highly demanded.

Up to now, various techniques have been reported to repair metal components, including arc welding [4], thermal spraying [5], and cold spraying [6]. Though arc welding can be used to repair cast irons, the dilution effect and distortion of

✉ Guijun Bi
gjb@simtech.a-star.edu.sg

Yongfeng Liu
liuyongfeng@bucea.edu.cn

Fei Weng
Weng_Fei@simtech.a-star.edu.sg

Youxiang Chew
chewyx@simtech.a-star.edu.sg

Shibo Liu
liu_shibo@simtech.a-star.edu.sg

Guangyi Ma
gyma@dlut.edu.cn

Seung Ki Moon
skmoon@NTU.edu.sg

¹ Beijing Key Laboratory of Performance Guarantee on Urban Rail Transit Vehicles, School of Mechanical-Electronic and Automobile Engineering, Beijing University of Civil Engineering and Architecture, Beijing 100044, China

² Joining Technology Group, Singapore Institute of Manufacturing Technology, 73 Nanyang Drive, Singapore 637662, Singapore

³ Key Laboratory for Precision and Non-traditional Machining Technology of Ministry of Education, School of Mechanical Engineering, Dalian University of Technology, Dalian 116023, China

⁴ Singapore Centre for 3D Printing, School of Mechanical and Aerospace Engineering, Nanyang Technological University, 50 Nanyang Avenue, Singapore 639798, Singapore

Table 1 Chemical compositions of the nodular cast iron substrate, Inconel 625, and SS420 powders

Elements	Fe	Ni	C	Si	Cr	Mn	Co	Mo	Al	Ti	NbTa	P	S
Cast iron	Bal.	≤0.08	3.0–3.5	2.0–2.6	0.1–0.6	0.4–0.7	0.3–0.5	≤0.1	≤0.1	≤0.05	–	0.08	≤0.08
SS420	Bal.	≤0.6	0.35	≤0.5	13.0	≤0.6	≤0.75	≤0.75	–	–	–	–	–
Inconel 625	5.0	Bal.	0.1	0.5	20.0–23.0	0.5	1.0	8.0–10.0	0.4	0.4	3.15–4.15	0.015	0.015

the substrate is the main challenge. Moreover, the process parameters should be carefully selected [1]; otherwise, new cracks would form during the repair process. As to thermal spraying and cold spraying, the inferior bonding strength is a most concerned issue. In recent days, laser cladding [7–9] and laser-based additive manufacturing [10–14] techniques have been proven feasible for deposition of various kinds of materials and applicable for repair purpose. Different self-fluxing alloys [15], Ni-base alloy [16], Co-base alloy [17], Fe-base alloy [18], tungsten carbide (WC) [19], and some composite materials systems (e.g., Ni-Ti-C [20]) have been reported in laser cladding on cast irons. However, no attempt has been made to deposit functionally graded layers on cast iron, to achieve nearly defect free repair and meanwhile maintain the inherent properties of the substrate.

It is noteworthy that Ni-base alloy has good compatibility with the Fe-base alloys owing to the formation of Ni/Fe infinite solid solution. As mentioned above, laser cladding Ni-base alloy on cast iron has been reported. Due to the high chromium and carbon content, stainless steel 420 (SS420) exhibits excellent corrosion resistance and superior wear resistance, which has been used in repair of some critical materials, such as 300M steel, an aero-grade ultra-high-strength steel aircraft material [21]. Nevertheless, the application of SS420 in repair of cast iron is rarely reported. However, as a martensitic stainless steel, SS420 has limited weldability due to the high hardenability and susceptibility to hydrogen induced or cold cracking [22]. Hence, deposition of SS420 by welding requires both preheat and post-weld heat treatment to suppress cracking and improve the final mechanical properties [22, 23].

In this paper, a novel Inconel 625/SS420 functionally graded material (FGM) is fabricated on a cast iron by laser-aided

additive manufacturing (LAAM). The process is developed without preheating and post-heating to simplify the deposition process. By introducing Inconel 625 as a buffer layer, potential cracks are expected to be eliminated. The usage of SS420 is beneficial to retain the inherent wear properties of cast iron substrate. Microstructure and wear properties of the deposited FGM are intensively analyzed.

2 Materials and methods

Nodular cast iron was used as the substrate material. Ni-base superalloy (Inconel 625) powders and stainless steel 420 (SS420) powders were employed as the deposition materials. During LAAD, an Inconel 625 layer was prepared on the cast iron substrate as a buffer layer and then three layers of SS420 were deposited on the buffer layer. The thickness of each layer was controlled to around 1.0 mm. The nominal compositions of the substrate and deposition powders are listed in Table 1.

LAAM process was carried out on a self-developed 6-kW fiber laser system equipped with a robot. The laser beam was guided through an optical fiber from the laser machine to the work place and focused by an optic with 200 mm focal length. The powder feeding was achieved by using a Sulzer Metco TWIN 10 C powder feeder and a conical powder feeding nozzle. The coaxial powder nozzle guaranteed a homogeneous powder distribution in the laser/powder interaction zone. The LAAM process parameters were carefully selected to eliminate obvious defects (e.g., pores or cracks) in the deposited samples. In the present study, the optimized process parameters were as follows: laser power 1.5 kW, beam size

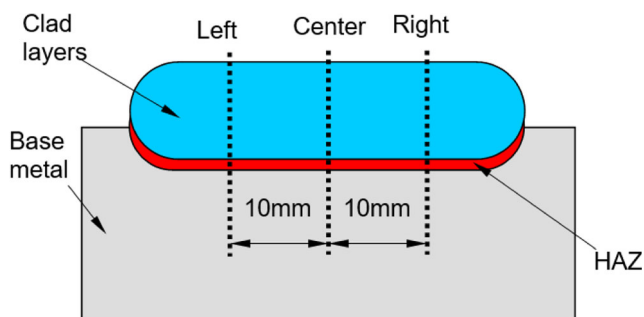


Fig. 1 Distribution of hardness indentations

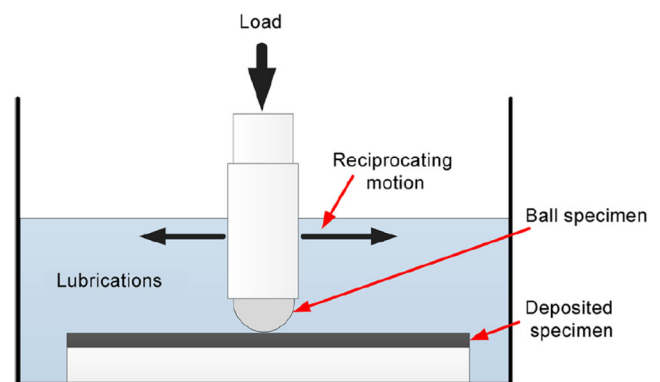


Fig. 2 Schematic diagram of the reciprocating ball-on-flat wear test [24]

Table 2 Test conditions for dry and lubricated wear test

Wear test type	Stroke length, mm	Load, N	Reciprocating frequency, Hz	Test time, s	Sliding distance, m
Dry	10	25	5	1000	100
Lubricated	10	200	10	2000	400

3 mm, scanning velocity 600 mm/s, powder feed rate 13.5 g/min (Inconel 625), and 12.8 g/min (SS420). The interlayer temperature was maintained at 175 °C.

One batch of samples was deposited and then cross-sectioned, polished, and etched. The etching reagent was Kalling's solution (40 ml HCl, 40 ml ethanol, and 2 g cupric chloride). Microstructures of the LAAM specimens were investigated by optical microscopy (OM), scanning electron microscopy (SEM, Philips/FEI XL30; JEOL 6400), and energy dispersive X-ray (EDX). Micro-hardness test was carried out using a LECO M-400 Vickers hardness tester under a load of 0.3 kg for 15 s. Three lines (left, center, and right) in total were tested in the cross section of the deposited specimens, as shown in Fig. 1. The three values at the same distance from the top surface were averaged. The micro-hardness distributions were obtained by the test results from the top of the SS420 layer, via Inconel 625 layer, heat affected zone (HAZ), down to cast iron substrate.

The top surface of the other batch of deposited samples was polished to a 0.05- μm finish. Both dry and lubricated sliding wear tests were carried out based on the ASTM standard G 133-02 using a linear, reciprocating ball-on-flat wear tester, and the diagram of which is shown in Fig. 2 [24]. Mobile

DTE oil was used for the lubricated wear test and the sample was fully immersed under the lubrications during the test. The 440C stainless steel ball (SS440C, diameter 9.5 mm, hardness 750 HV) was used as the wear counterpart. The direction of the relative motion between the spherical tip of the ball and the polished specimen surface reversed in a periodic fashion such that the sliding occurred back and forth in a straight line. The coefficient of friction (COF) was synchronously recorded. The test conditions for dry and lubricated wear tests are listed in Table 2.

The wear surface morphologies were analyzed by SEM and EDX. Cross-sectional profile of each wear track was measured at three different locations using an Alicona optical 3D non-contact metrology system. Wear volume (V_f , mm^3) was calculated by the equation below, based on which specific wear volume rate (mm^3/Nm) could be further calculated:

$$V_f = A \times L$$

- A Average cross-sectional area of the wear track, mm^2
 L Length of stroke, mms

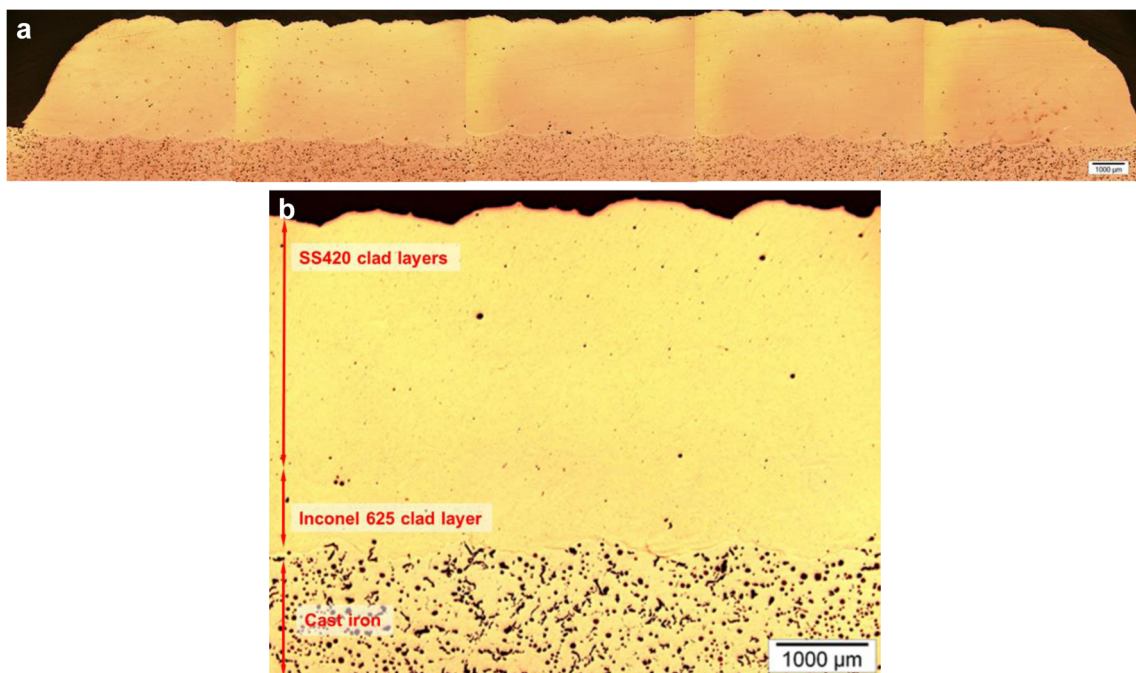


Fig. 3 Cross-sectional view of the deposited sample. **a** Overview of the whole interface. **b** Local view with higher magnification

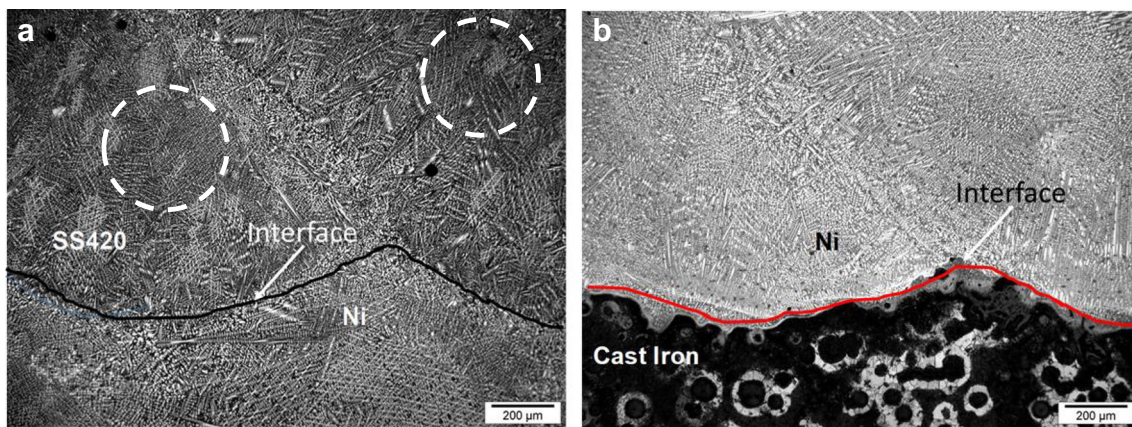


Fig. 4 Interfacial characteristics of SS420 layers/Inconel 625 layer (a) and Inconel 625 layer/cast iron substrate (b)

3 Results and discussion

3.1 Macrostructure

Figure 3 shows the cross-sectional view of the deposited sample. Results indicate that the Ni-base layer and the cast iron substrate show very compact metallurgical bonding feature with very low porosity. No cracks appear at the interface and in both the substrate and deposited layers. Due to the low heat input to the substrate in LAAM process, formation of cracks in cast iron can be restrained. Besides, the Ni-base alloy layer acts as a buffer layer between the SS420 and the cast iron substrate, which is beneficial to obtain crack-free deposition layers. As reported by Lestan et al. [25], the cracks in the deposited Metco 15 E Ni-base layers were not eliminated completely even with preheating of the cast iron substrate. In the present paper, the Inconel 625 Ni-base alloy is proved appropriate as a buffer layer material to further deposit SS420 layers. Furthermore, the Inconel 625 Ni-base alloy with low melting point can help minimize the porosity which are mainly caused by the burning of abundant carbon existing in the cast iron [26].

3.2 Microstructure

Figure 4a, b illustrates the interfacial microstructure of the SS420 layers/Inconel 625 layer and Inconel 625 layer/cast iron substrate, respectively. The results further verify the crack-free interfaces.

Either the SS420 layers or the Inconel 625 layer shows similar microstructure, which is dominated by columnar dendrites. Some of the long dendrites grow along the direction of heat flow, which is more obvious near the Inconel 625 layer/cast iron interface that the dendrites grow upwards vertical to the interface (Fig. 4b). This can be attributed to the unidirectional heat flow to substrate during the deposition of the single Inconel 625

layer. However, the columnar dendrites exhibit various grow directions (see Fig. 4a, in dashed circles) during the solidification into the central section far from the boundaries, probably owing to the homogeneous nucleation and Marangoni convection effect [27]. The fine multidirectional columnar dendrites are beneficial to property improvement compared with unidirectional coarse microstructure.

Further observation demonstrates that the columnar dendrites in SS420 layers have primary dendrite arm spacing around 10–20 μm, as shown in Fig. 5. Along with the rapid heating and cooling rate in LAAM, the columnar dendrites have limited time to grow up and growth of the massive columnar dendrites is restricted once they touch with each other. The fine columnar dendrites are beneficial to the properties of the final deposited FGM. EDX results show a Cr segregation phenomenon at the inter-dendrite position, which can be ascribed to the formation of Cr carbides [28]. The carbides can act as reinforcements in the FGM, resulting in high hardness.

3.3 Micro-hardness

Figure 6 shows the micro-hardness distributions of the deposited FGM. Slightly higher micro-hardness is formed in the HAZ, owing to the formation of high-carbon martensite and ledeburite [16]. Moreover, the hardness undergoes a smooth transition from the HAZ to the SS420 layers, owing to the Inconel 625 layer, acting as a buffer layer between SS420 layers and cast iron substrate. The hardness of the SS420 layers reaches 620–650 HV_{0.3}. Hence, the FGM shows a superior gradient micro-hardness distribution similar with the carburized or nitrided steel components [29, 30]. This is beneficial to the improvement of wear property.

The micro-hardness decreases slightly from the Inconel 625/SS420 interface to the FGM free surface. Similar

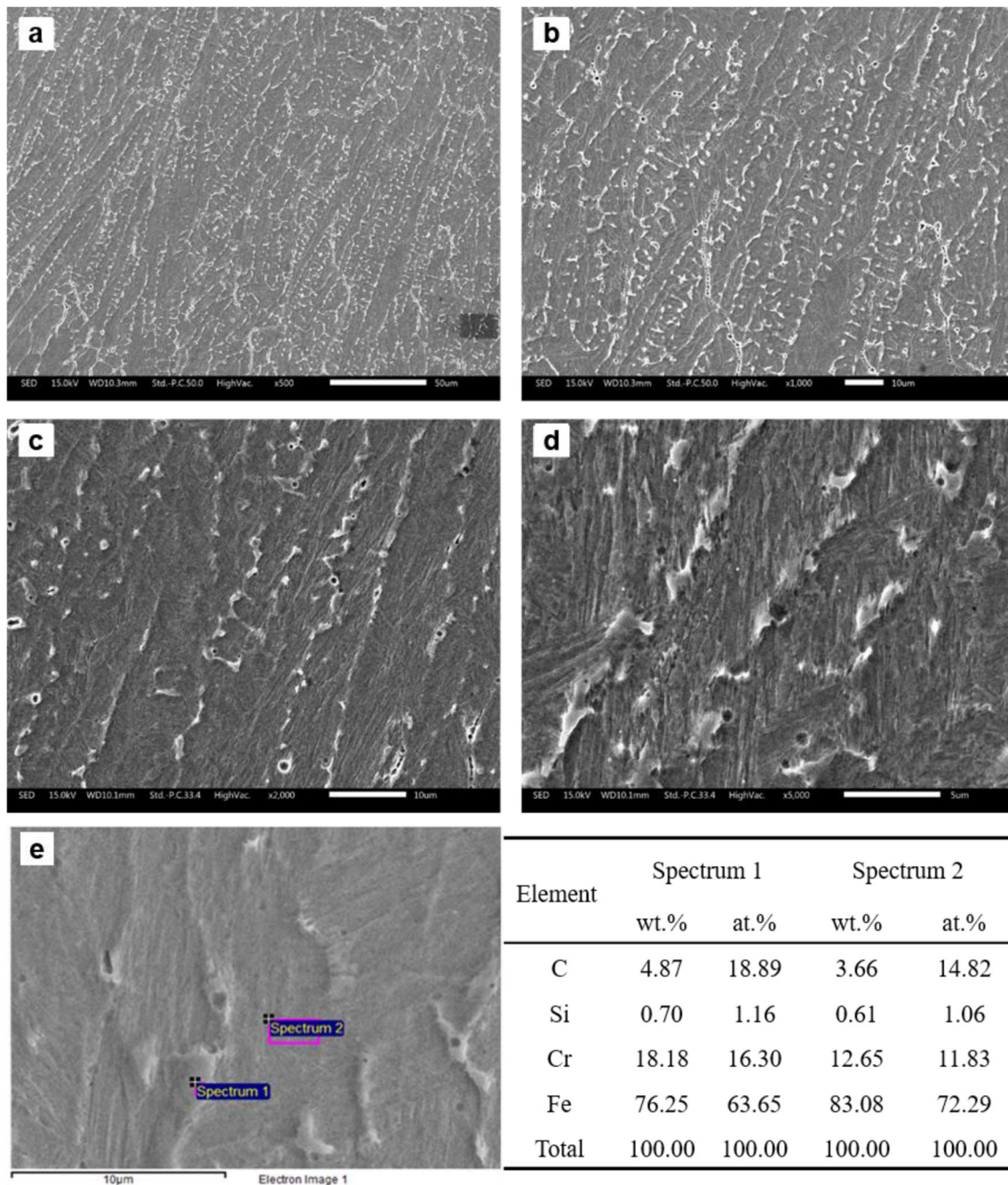


Fig. 5 Morphologies of the columnar dendrites in SS 420 layers at different magnifications (a–d) and EDX analysis results of the dendrite and interdendrite positions (e). Remark: the micro images were taken from the upper SS420 layer

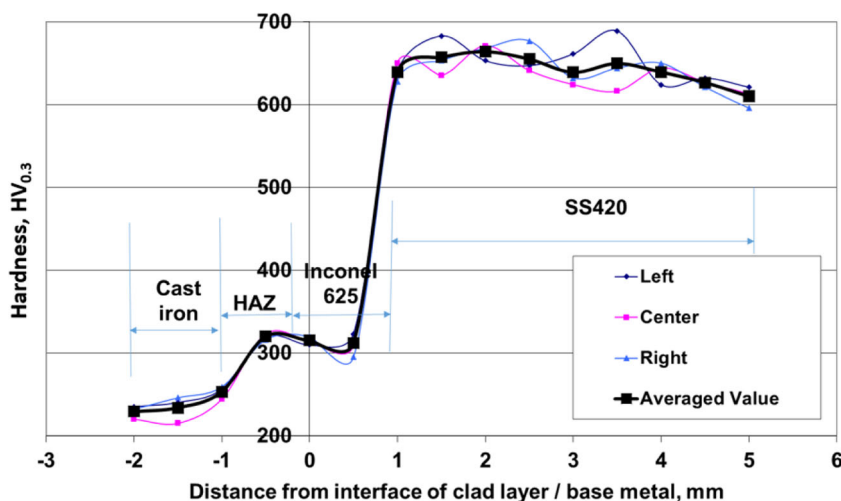
phenomenon was reported by Liu et al. [16] in multi-layer laser cladding of NiCoCr alloy on compacted graphite cast iron and it was attributed to the decreasing dilution effect of C from the substrate. However, in the present study, the deposited SS420 layers were separated from the high-carbon cast iron substrate. Therefore, the lower micro-hardness at surface layer than the internal layer can be ascribed to the formation of residual austenite under rapid cooling rate [31]. The internal layers are subject to in situ tempering effect of

subsequent layers, demonstrating higher micro-hardness due to the decomposition of residual austenite and formation of martensite and carbides.

3.4 Wear property

Figure 7 shows the COF and wear volume loss of the deposited specimens under dry and lubricated sliding wear conditions. It is evident that there is an initial stage and a steady

Fig. 6 Hardness distributions of the deposited layers, HAZ, and cast iron substrate



stage for both kinds of wear test, as shown in Fig. 7a. Under dry wear test, the COF initially increases rapidly until 100 s, then decreases by 200 s and finally stabilizes at about 0.7. However, the COF fluctuates obviously. On the contrary, very little fluctuation can be observed in the COF curve under lubricated condition, and the COF stabilized at about 0.1. As shown in Fig. 7b, the wear volume loss under dry and

lubricated sliding wear is 0.04785 mm³ and 0.01451 mm³, respectively. Although much higher load and doubled sliding time is applied, the wear volume loss under lubricated condition is only about 1/3.3 of that under dry wear condition. Compared with the report of laser clad SS420 coatings on 300M steel [21], the Inconel 625/SS420 FGM developed on nodular cast iron shows superior wear resistance. The specific wear volume loss rate is 30.0×10⁻⁶ and 19.1×10⁻⁶ mm³/Nm, for ref. [21] and our dry sliding wear result respectively. During dry wear test, severe wear occurred, as the specimen surface contacted directly with the SS440C counterpart ball with 750 HV hardness. While under lubricated wear test, the thin lubrication layer between the FGM specimen and the wear counterpart acted as a protective layer, reducing COF and suppressing the wear process.

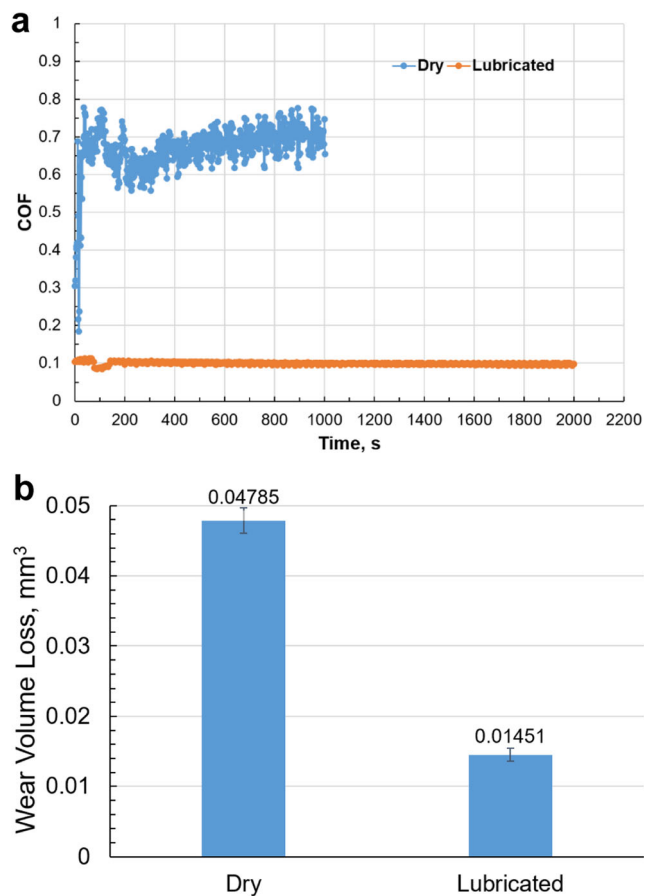


Fig. 7 COF (a) and wear volume loss (b) of the FGM under dry and lubricated wear conditions

Figure 8 shows the wear tracks and the corresponding cross-section profiles after dry wear and lubricated wear, respectively. The cross-section profiles were used to estimate the wear volume. It is obvious that the worn surface after dry wear shows black and brown feature, which can be attributed to oxidation. Further analysis verifies the oxidation during dry wear.

To further discuss the wear mechanism, the worn surface morphologies were analyzed by SEM and EDX, as shown in Fig. 9 and Table 3. The worn surface after dry wear test is dominated by plowing grooves and spalling (Fig. 9a–c). In comparison, the worn surface after lubricated wear is much smoother but severe spalling occurs regionally (Fig. 9d–f). As aforementioned, the wear counterpart ball is harder than the deposited FGM and the sample is subjected to plowing by the micro asperities on the ball surface. Moreover, the alternating stress existed at the sample surface, resulting in crack formation and propagating and further causing spalling. Though the load was low in the dry wear test, spalling appeared almost on the entire worn surface. Because the groves formed by plowing can act as crack initiation. However, the worn surface after lubricated wear showed severe regional spalling, which

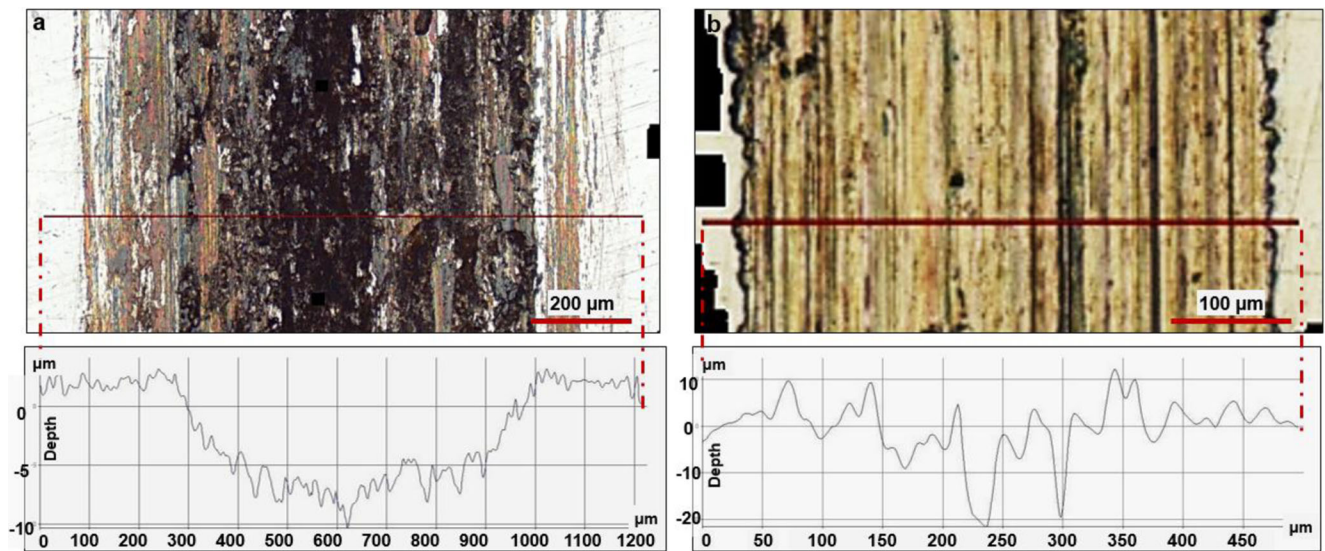


Fig. 8 Wear tracks observed by 3D non-contact metrology system and the corresponding cross-section profiles after dry sliding wear (a) and lubricated sliding wear (b)

can be attributed to the applied high load. Severe plastic deformation (Fig. 9e) and work hardening occurred on the sample surface under the effect of high load. Hence, the plowing effect from the counterpart ball can be suppressed during the lubricated wear, resulting in smoother worn surface (Fig. 9d–f). However, once micro-cracks (Fig. 9f) formed under the effect of high alternating stress, they would propagate rapidly and cause severe spalling.

As shown in Table 3, extremely high oxygen and iron content was observed on the dry worn surface, indicating

that severe oxidation occurred during the dry wear test. During dry wear tests, friction heat accumulated and resulted in high temperature at micro-zones [32]. Therefore, the sample surface, directly exposed to ambient atmosphere, was oxidized easily. The oxides can act as a third-body and cause three-body wear [33]. The fluctuation of COF in dry wear (Fig. 7a) can be partially attributed to the dynamic formation and peeling-off of the oxides between the sliding surfaces [34]. During lubricated wear, the sliding surface was isolated from the ambient air

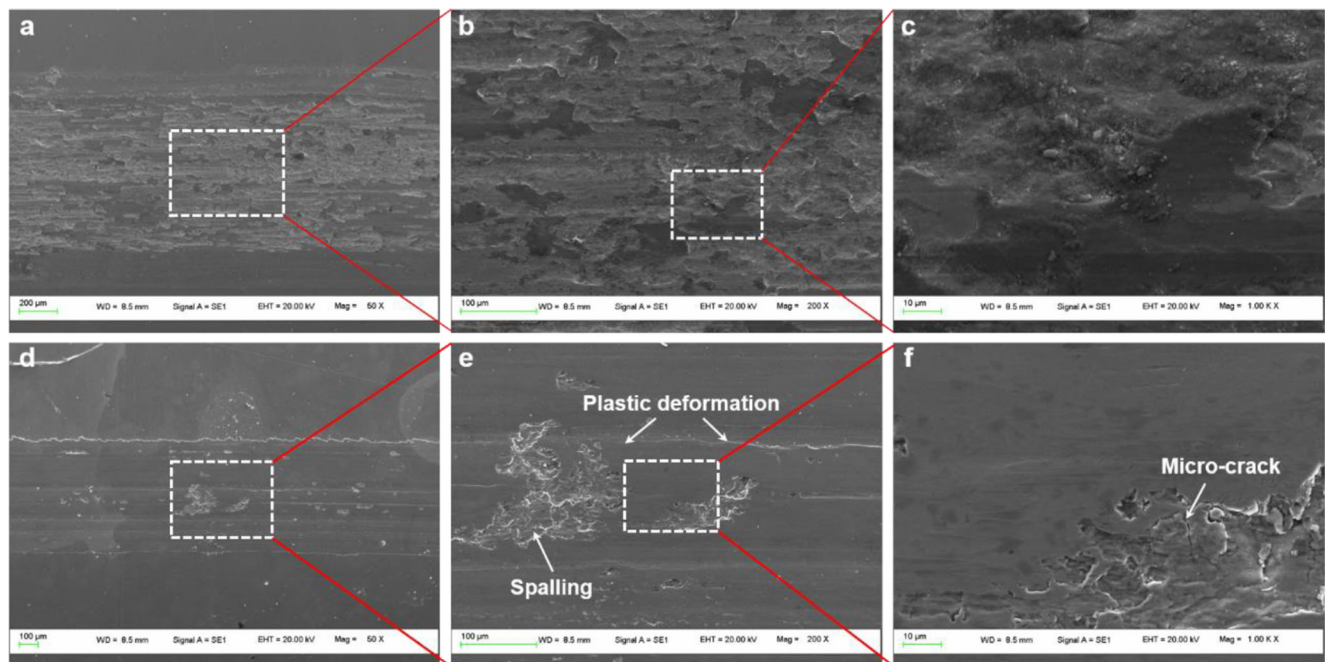
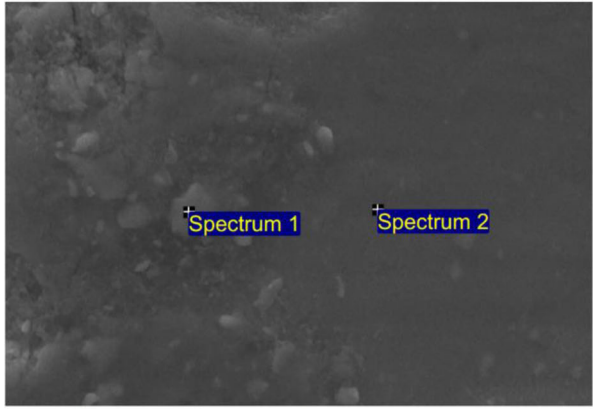


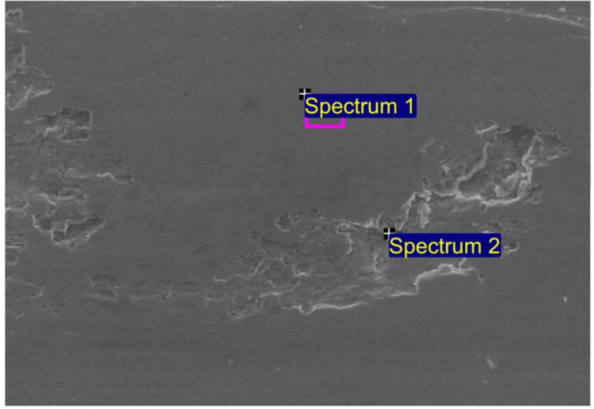
Fig. 9 Worn morphologies of the specimens after dry sliding wear (a–c) and lubricated sliding wear (d–f)

Table 3 EDX analysis results of the samples after dry sliding wear and lubricated sliding wear

Element	Dry wear				Lubricated wear			
	Spectrum 1		Spectrum 2		Spectrum 1		Spectrum 2	
	wt.%	at.%	wt.%	at.%	wt.%	at.%	wt.%	at.%
C	4.4	12.32	3.21	8.96	10.74	34.36	28.47	61.22
O	19.58	41.11	21.51	45.10	1.75	4.21	4.62	7.46
Si	0.51	0.61	0.28	0.34	0.50	0.69	0.32	0.30
P	-	-	0.06	0.06	0.13	0.16	0.13	0.11
S	0.07	0.07	0.04	0.04	0.33	0.40	0.04	0.04
Cr	10.94	7.07	11.23	7.24	11.76	8.69	9.03	4.49
Mn	0.30	0.18	0.15	0.09	0.30	0.21	0.49	0.23
Fe	64.17	83.08	63.53	38.17	74.45	51.25	55.97	25.89
Ni	0.02	0.01	-	-	0.05	0.03	0.17	0.08
Mo	-	-	-	-	-	-	0.75	0.20
Total	100.00		100.00		100.00		100.00	



10µm Electron Image 1



100µm Electron Image 1

and oxidation was restrained significantly. Moreover, the lubricant can also function as coolant during the regional work hardening. This could further enhance the work hardening effect. To sum up, the deposited Inconel 625/SS420 FGM exhibits good wear resistance, especially under lubricated wear.

4 Conclusions

Inconel 625/SS420 FGM was successfully deposited on nodular cast iron by LAAM. The microstructure, micro-hardness, and wear property were analyzed. Based on the results and discussion, conclusions can be drawn as follows:

- LAAM process is suitable to produce FGMs to repair nodular cast iron.

- Inconel 625 Ni-base alloy is a good candidate as a buffer layer between nodular cast iron and SS420 to achieve crack-free deposition with minimum porosity.
- The gradient micro-hardness distribution corresponds well with the materials used for deposition of the functionally graded layers.
- Fine columnar dendritic microstructure can form after LAAM due to the limited heat input and rapid cooling rate.
- The Inconel 625/SS420 FGM has good wear resistance, especially under lubricated condition.

Funding information The author Yongfeng Liu was financially supported by the Beijing Municipal Natural Science Foundation (3192011) for his part of contribution to this paper.

Publisher's note Springer Nature remains neutral with regard to jurisdictional claims in published maps and institutional affiliations.

References

- Mirhedayatian SM, Vahdat SE, Jelodar MJ, Saen RF (2013) Welding process selection for repairing nodular cast iron engine block by integrated fuzzy data envelopment analysis and TOPSIS approaches. *Mater Des* 43:272–282. <https://doi.org/10.1016/j.matdes.2012.07.010>
- de Sousa JA, Sales WF, Guesser WL, Machado ÁR (2018) Machinability of rectangular bars of nodular cast iron produced by continuous casting. *Int J Adv Manuf Technol* 98:2505–2517. <https://doi.org/10.1007/s00170-018-2387-x>
- Han S, Huh H (2012) Evaluation of a cast-joining process of dual-metal crankshafts with nodular cast iron and forged steel for medium speed diesel engines. *Int J Adv Manuf Technol* 63:319–327. <https://doi.org/10.1007/s00170-012-3909-6>
- Sadeghi A, Moloodi A, Golestanipour M, Mahdavi Shahri M (2017) An investigation of abrasive wear and corrosion behavior of surface repair of gray cast iron by SMAW. *J Mater Res Technol* 6:90–95. <https://doi.org/10.1016/j.jmrt.2016.09.003>
- Tan JC, Looney L, Hashmi MSJ (1999) Component repair using HVOF thermal spraying. *J Mater Process Technol* 92–93:203–208. [https://doi.org/10.1016/S0924-0136\(99\)00113-2](https://doi.org/10.1016/S0924-0136(99)00113-2)
- Champagne V, Helfrich D (2015) Critical assessment 11: structural repairs by cold spray. *Mater Sci Technol Lond* 31:627–634. <https://doi.org/10.1179/1743284714Y.0000000723>
- Weng F, Chen C, Yu H (2014) Research status of laser cladding on titanium and its alloys: a review. *Mater Des* 58:412–425. <https://doi.org/10.1016/j.matdes.2014.01.077>
- Sun SD, Barr C, Brandt M (2018) In situ control of tempered martensite during laser cladding repair of aero-grade 300M steel using AISI 420 stainless steel powder. *J Laser Appl* 30:032502. <https://doi.org/10.2351/1.5040629>
- Aghasibeig M, Fredriksson H (2012) Laser cladding of a featureless iron-based alloy. *Surf Coat Technol* 209:32–37. <https://doi.org/10.1016/j.surfcoat.2012.08.013>
- Bi G, Ng GKL, Teh KM, Jarfors AE (2010) Feasibility study on the laser aided additive manufacturing of die inserts for liquid forging. *Mater Des* 31:S112–S116. <https://doi.org/10.1016/j.matdes.2009.10.039>
- Zheng B, Topping T, Smugeresky JE, Zhou Y, Biswas A, Baker D, Lavernia EJ (2010) The influence of Ni-coated TiC on laser-deposited IN625 metal matrix composites. *Metall Mater Trans A* 41:568–573. <https://doi.org/10.1007/s11661-009-0126-5>
- Mok SH, Bi G, Folkes J, Pashby I (2008) Deposition of Ti-6Al-4V using a high power diode laser and wire, part I: investigation on the process characteristics. *Surf Coat Technol* 202:3933–3939
- Mok SH, Bi G, Folkes J, Pashby I, Segal J (2008) Deposition of Ti-6Al-4V using a high power diode laser and wire, part II: investigation on the mechanical properties. *Surf Coat Technol* 202:4613–4619. <https://doi.org/10.1016/j.surfcoat.2008.03.028>
- Bi G, Gasser A (2011) Restoration of nickel-base turbine blade knife-edges with controlled laser aided additive manufacturing. *Phys Procedia* 12:402–409. <https://doi.org/10.1016/j.phpro.2011.03.051>
- Tong X, Li F, Liu M, Dai M, Zhou H (2010) Thermal fatigue resistance of non-smooth cast iron treated by laser cladding with different self-fluxing alloys. *Opt Laser Technol* 42:1154–1161. <https://doi.org/10.1016/j.optlastec.2010.03.001>
- Liu H, Hao J, Han Z, Yu G, He X, Yang H (2016) Microstructural evolution and bonding characteristic in multi-layer laser cladding of NiCoCr alloy on compacted graphite cast iron. *J Mater Process Technol* 232:153–164. <https://doi.org/10.1016/j.jmatprotec.2016.02.001>
- Ocelik V, de Oliveira U, de Boer M, de Hosson JTM (2007) Thick Co-based coating on cast iron by side laser cladding: analysis of processing conditions and coating properties. *Surf Coat Technol* 201:5875–5883. <https://doi.org/10.1016/j.surfcoat.2006.10.044>
- Weng Z, Wang A, Wang Y, Xiong D, Tang H (2016) Diode laser cladding of Fe-based alloy on ductile cast iron and related interfacial behavior. *Surf Coat Technol* 286:64–71. <https://doi.org/10.1016/j.surfcoat.2015.12.031>
- Yilbas BS, Akhtar SS, Karatas C, Boran K (2016) Laser treatment of dual matrix cast iron with presence of WC particles at the surface: influence of self-annealing on stress fields. *Opt Laser Technol* 76:6–18. <https://doi.org/10.1016/j.optlastec.2015.07.003>
- Cui C, Guo Z, Wang H, Hu J (2007) In situ TiC particles reinforced grey cast iron composite fabricated by laser cladding of Ni-Ti-C system. *J Mater Process Technol* 183:380–385. <https://doi.org/10.1016/j.jmatprotec.2006.10.031>
- Da Sun S, Fabijanic D, Barr C, Liu Q, Walker K, Matthews N, Orchowski N et al (2018) In-situ quench and tempering for microstructure control and enhanced mechanical properties of laser clad AISI 420 stainless steel powder on 300M steel substrates. *Surf Coat Technol* 333:210–219. <https://doi.org/10.1016/j.surfcoat.2017.10.080>
- Baghjari SH, Akbari Mousavi SAA (2013) Effects of pulsed Nd:YAG laser welding parameters and subsequent post-weld heat treatment on microstructure and hardness of AISI 420 stainless steel. *Mater Des* 43:1–9. <https://doi.org/10.1016/j.matdes.2012.06.027>
- Branza T, Deschaux-Beaume F, Sierra G, Lours P (2009) Study and prevention of cracking during weld-repair of heat-resistant cast steels. *J Mater Process Tech* 209:536–547. <https://doi.org/10.1016/j.jmatprotec.2008.02.033>
- Bajwa R, Khan Z, Nazir H, Chacko V, Saeed A (2016) Wear and friction properties of electrodeposited Ni-based coatings subject to nano-enhanced lubricant and composite coating. *Acta Metall Sin (Engl Lett)* 29:902–910. <https://doi.org/10.1007/s40195-016-0470-6>
- Lestan Z, Milfelner M, Balic J, Brezocnik M, Karabegovic I (2013) Laser deposition of Metco 15E, Colmony 88 and VIM CRU 20 powders on cast iron and low carbon steel. *Int J Adv Manuf Technol* 66:2023–2028. <https://doi.org/10.1007/s00170-012-4478-4>
- Yan SX, Dong SY, Xu BS, Wang YJ, Ren WB, Fang JX (2014) Effect of molten pool convection on pores and elements distribution in the process of laser cladding. *Infrared Laser Eng* 43:2832–2839. <https://doi.org/10.3969/j.issn.1007-2276.2014.09.009>
- Yadollahi A, Shamsaei N, Thompson SM, Seely DW (2015) Effects of process time interval and heat treatment on the mechanical and microstructural properties of direct laser deposited 316L stainless steel. *Mater Sci Eng A* 644:171–183. <https://doi.org/10.1016/j.msea.2015.07.056>
- Baghjari SH, AkbariMousavi SAA (2014) Experimental investigation on dissimilar pulsed Nd:YAG laser welding of AISI 420 stainless steel to kovar alloy. *Mater Des* 57:128–134. <https://doi.org/10.1016/j.matdes.2013.12.050>
- Sun Z, Zhang CS, Yan MF (2014) Microstructure and mechanical properties of M50NiL steel plasma nitrocarburized with and without rare earths addition. *Mater Des* 55:128–136. <https://doi.org/10.1016/j.matdes.2013.09.030>
- Cheng X, Xie C (2003) Effect of rare earth elements on the erosion resistance of nitrided 40Cr steel. *Wear* 254:415–420. [https://doi.org/10.1016/S0043-1648\(03\)00018-8](https://doi.org/10.1016/S0043-1648(03)00018-8)
- Barlow LD, Du Toit M (2012) Effect of austenitizing heat treatment on the microstructure and hardness of martensitic stainless steel AISI 420. *J Mater Eng Perform* 21:1327–1336. <https://doi.org/10.1007/s11665-011-0043-9>
- Quinn TFJ (1983) Review of oxidational wear: part I: the origins of oxidational wear. *Tribol Int* 16:257–271. [https://doi.org/10.1016/0301-679X\(83\)90086-5](https://doi.org/10.1016/0301-679X(83)90086-5)
- Gates JD (1998) Two-body and three-body abrasion: a critical discussion. *Wear* 214:139–146. [https://doi.org/10.1016/S0043-1648\(97\)00188-9](https://doi.org/10.1016/S0043-1648(97)00188-9)
- Cui XH, Wang SQ, Wang F, Chen KM (2008) Research on oxidation wear mechanism of the cast steels. *Wear* 265:468–476. <https://doi.org/10.1016/j.wear.2007.11.015>